

Medical University of Varna
Faculty of Pharmacy

Yoana Nikolova Sotirova

**Nanostructured Lipid Carriers Loaded with
Hypericum perforatum L. Extract for Dermal Application and
Accelerated Wound Healing**

Extended Abstract of a PhD Thesis

Scientific Supervisors:

Prof. Kaloyan Georgiev, PhD, DSc
Assoc. Prof. Velichka Andonova, PhD

Varna, 2024

I. Introduction

Wound care is a significant global health issue affecting millions annually, with wound healing being a complex physiological process influenced by various factors. Current treatments often fail to create an optimal healing environment, prompting the search for new, more effective therapeutic agents. St. John's wort (*Hypericum perforatum* L.), known for treating mental health disorders and skin conditions, owes much of its pharmacological efficacy to hyperforin—a biologically active but structurally unstable compound. Stabilizing hyperforin through inclusion in nanostructured lipid carriers (NLCs) offers a promising solution. NLCs, being biocompatible, biodegradable, and capable of high drug loading, are ideal for skin applications. Their incorporation into semi-solid dosage forms like bigels further enhances therapeutic effectiveness by prolonging skin contact. Bigels, known for their favorable texture, hydration properties, and patient compliance, optimize drug delivery to the skin. This thesis explores the development of hyperforin-rich St. John's wort extract-loaded NLCs within bigels as a novel strategy for promoting accelerated wound healing.

II. Aim and Objectives

Aim

The present thesis aims to develop nanostructured lipid carriers containing St. John's wort extract for dermal application and accelerated wound healing.

Objectives

To achieve the stated goal, the following objectives were set:

1. Preparation of St. John's wort extract rich in hyperforin (HP).
 - 1.1. Development of a maceration method suitable with limited influence of light and atmospheric oxygen.
 - 1.2. Qualitative and quantitative analysis of hyperforin content in the obtained St. John's wort extracts.
2. Development and characterization of nanostructured lipid carriers (NLCs) loaded with HP-rich St. John's wort extract.
 - 2.1. Development of "blank" NLCs by high-shear homogenization followed by ultrasonication while varying the solid lipids (glyceryl behenate (GB), beeswax (BW)), liquid oils (borage oil (BO), almond oil (AO)), and experimental conditions (homogenization speed and ultrasonication duration and temperature).
 - 2.2. Characterization of "blank" NLCs in terms of visual appearance, particle size and particle size distribution, zeta potential, degree of crystallinity, and physical stability. Selection of suitable carriers for incorporation of HP-rich St. John's wort extract.
 - 2.3. Preparation of HP-rich St. John's wort extract-loaded NLCs and characterization in terms of appearance, particle size and particle size distribution, zeta potential, changes in polymorphic modifications, entrapment efficiency, stability, *in vitro* antimicrobial efficacy and antiviral activity.
3. Development and characterization of a semi-solid dosage form (bigel) incorporating NLCs loaded with HP-rich St. John's wort extract.
 - 3.1. Development of "blank" bigels with gelling agents poloxamer 407 and sorbitan monostearate and bigels containing HP-rich St. John's wort extract-loaded NLCs.

- 3.2. Characterization of “blank” and loaded biphasic gels in terms of visual appearance, homogeneity, pH, physical stability, mechanical properties (spreadability, hardness, adhesiveness, and cohesiveness), and rheological behavior.
4. *In vivo* study of the wound-healing potential of the prepared final semi-solid dosage form on an excision wound model in experimental animals.
 - 4.1. Monitoring the dynamics of tissue repair based on changes in the wound size over time.
 - 4.2. Determination of plasma antioxidant status (antioxidant capacity and degree of oxidative stress).

III. Methods

1. Preparation and chromatographic analysis of hyperforin-rich St. John’s wort extract

The extract was prepared via maceration of 30.0 g of St. John’s wort chopped aerial parts with anhydrous dichloromethane in a tightly sealed, 250 mL amber borosilicate flask. The extraction was carried out in the dark, with prior deaeration of the maceration medium with argon flow for 30 min. After 48 h, the obtained extract was vacuum-filtered through a sintered borosilicate glass filter, and the solvent was removed under reduced pressure using a rotary evaporator. The final extract was stored at -20 °C. Two extracts were produced, differing in the plant mass-to-solvent ratio used—30:75 and 30:100 (w/v; g/mL).

The HPLC analysis was performed using a Thermo Scientific UltiMate 3000 high-performance liquid chromatograph equipped with a variable UV/Vis detector. The mobile phase, composed of 0.3% phosphoric acid and acetonitrile (10:90, v/v), was applied isocratically over 12 min at a flow rate of 0.8 mL/min. The temperature of the chromatographic column and the autosampler were maintained at 25 and 10 °C, respectively. The sample injection volume was 20.0 µL. The eluent composition was determined by UV/Vis detection at a wavelength of 273 nm, and the data was processed using specialized Chromeleon™ 7.2. software¹. The St. John’s wort extracts were dissolved in anhydrous methanol to 20.0 µg/mL immediately before analysis. The resulting samples were filtered through a syringe filter (0.20 µm) and analyzed six-fold¹. The presence of HP was determined by the retention time. The absolute calibration method was used for the identification of the analyte, for its quantitative analysis, and for the determination of the extraction yield. For the purposes of the analysis, a certified HP standard and a commercial supercritical CO₂ extract were used.

2. Preparation and characterization of nanostructured lipid carriers

2.1. Preparation of the nanostructured lipid carriers

The composition of lipid nanocarriers included the following components:

- Solid lipid—white beeswax (BW) or glyceryl behenate (GB);
- Liquid lipid—almond oil (AO) or borage oil (BO);
- Surfactants—polyoxyethylene (20) sorbitan monooleate (PSMO) and sorbitan monooleate (SMO).

The NLCs were prepared with a 10% (w/w) lipid phase concentration at a solid-to-liquid lipid ratio of 7:3 and a surfactant mixture (5%, w/w) in a PSMO-to-SMO ratio of 3:2. The method involved sequential emulsification, high-shear homogenization (10,000 and 15,000 rpm), and ultrasonication (at 4 and 25 °C for 5 and 15 min). The aqueous phase (double-distilled and PSMO) was heated to

¹ Stefanov, S., Stoeva, S., Georgieva, S., Hristova, M., Nikolova, K., Dobрева, M., Andonova, V. (2022) ‘In vivo comparative assessment of incised wound healing in rats after application of hydrogel/organogel formulation containing St. John’s wort methanol extract’, *Bulgarian Chemical Communications*, 54, 46-51.

80 ± 2 °C and added dropwise to the lipid phase (solid lipid, liquid lipid, and SMO) heated to the same temperature under continuous stirring at a speed of 750 rpm for 3 min. The resulting macroemulsion was homogenized for 3 min and then ultrasonified. HP-rich St. John's wort extract-loaded samples (HP-NLCs) were prepared by incorporating the extract (1.25%, w/w) into the lipid phase before the emulsification under dark conditions.

2.2. Characterization of the nanostructured lipid carriers

Mean particle size, particle size distribution, and zeta potential

The mean particle size, polydispersity index, and zeta potential of the developed nanoparticles were investigated by dynamic (DLS) and electrophoretic light scattering (ELS) methods using Zetasizer Ultra. After a thousand-fold dilution of all samples with double-distilled water, particle size was evaluated through triplicate backscatter intensity measurements at 173°, while surface electric charge (zeta potential) was determined from light scattering at 13°.

Degree of crystallinity

X-ray diffraction analysis was conducted to monitor changes in the degree of crystallinity of solid lipids, solid-liquid lipid mixtures (obtained by homogenization after melting at 80 ± 2 °C in a 7:3 ratio), NLCs, HP-NLCs, and HP-rich St. John's wort extract. The analysis used a Panalytical Empyrean Diffractometer with a Cu-K α monochromator ($\lambda = 1.5406 \text{ \AA}$). Scans were performed over a 2–50° 2 θ range at a 1 s/step scanning speed and a step size of 0.013° 2 θ .

Physical stability during storage

NLC dispersions were stored at 4 °C for six months and were visually assessed monthly for possible signs of physical instability.

Entrapment efficiency

The entrapment efficiency (EE, %) of HP in the lipid nanocarriers was evaluated to determine the extract's actual content. For this analysis, 1.00 ± 0.01 g of each HP-NLC sample was centrifuged at 10,000 rpm for 30 minutes. The supernatant was removed, and the lipid fraction was dispersed in 10 mL of anhydrous methanol, diluted fifty-fold with the same solvent, and filtered using syringe filters (0.20 μm). HP content in the resulting samples was quantified using the previously described HPLC protocol, and EE was calculated accordingly:²

$$EE, \% = \frac{\text{practically established amount of HP (mg)}}{\text{theoretical amount of HP (mg)}} \times 100$$

Extract-lipid interactions

ATR-FTIR analysis was performed to establish the actual interaction between the extract and the lipid nanocarriers. In the study were included: HP-rich St. John's wort extract, NLC dispersions, and HP-NLC dispersions loaded with 1.25%, 2.50%, and 5.00% (w/w) extract. The "overloaded" samples (containing 2.50 and 5.00% extract) were prepared similarly to those loaded with 1.25% extract. All nanosuspensions were studied as air-dried thin films on microscope slides. ATR-FTIR spectra were recorded using a Tensor II FTIR spectrophotometer after 32 scans, and processed with OPUS 8.0 software. The analyses were performed at 21 °C and low relative humidity.

² Younis, H., Khan, H.U., Maheen, S., Saadullah, M., Shah, S., Ahmad, N., Alshehri, S., Majrashi, M.A.A., Alsalmi, A., Siddique, R., Andleeb, M., Shabbir, S., Abbas, G. (2023) 'Fabrication, Characterization and Biomedical Evaluation of a Statistically Optimized Gelatin Scaffold Enriched with Co-Drugs Loaded into Controlled-Release Silica Nanoparticles', *Molecules*, 28(13), 5233.

Shape and inner morphology

The shape, size, and morphology of the “blank” and extract-loaded nanoparticles were determined using an HRTEM JEOL JEM 2100 operating at an accelerating voltage of 200 kV. Each nanodispersion was deposited on a carbon-coated Cu grid and air-dried for 24 h before the study.

Antiviral effect

The Victoria strain of herpes simplex virus type 1 (HSV-1; National Centre for Infectious and Parasitic Diseases, Sofia) was propagated in a confluent MDBK cells monolayer³ in DMEM with 0.5% fetal calf serum, 100 IU/mL penicillin, and 100 µg/mL streptomycin as a maintenance medium. After incubation at 37°C and 5% CO₂, the viral stock was stored at -80°C. Its infectious titer was determined as 10^{8.5} cell culture infectious doses 50% (CCID50) in 1 mL.

Cytotoxicity assay

A confluent MDBK monolayer cultured in 96-well plates was treated with serial dilutions of the NLC/HP-NLC samples in a maintenance DMEM medium (0.1 mL per well, four wells per sample). After 48-h incubation at 37 °C and 5% CO₂, cell viability was assessed via the neutral red uptake assay. Cells were incubated with the dye at 37 °C for 3 h, washed with phosphate-buffered saline, and treated with 0.15 mL desorbing solution (1% glacial acetic acid and 49% ethanol in double-distilled water). Optical density at 540 nm was measured thrice, and cytotoxic concentration 50%⁴ and the maximum tolerated concentration⁵ of each nanodispersion were determined and compared to acyclovir as a reference.

Determination of infectious viral titers

Ten-fold falling dilutions of the virus-containing material in a DMEM medium were prepared immediately before the analysis. In 96-well plates, 0.1 mL of each dilution was added to four wells. After 1 h of adsorption, the unadsorbed virus was removed, and 0.1 mL of DMEM medium was added to each well. The plates were incubated at 37 °C and 5% CO₂ for 48 h. The viral infectious titer was assessed microscopically by observing cytopathic effects and confirmed using the neutral red uptake assay. The development of cytopathic effect for each viral dilution was calculated as follows:

$$100 - \left[\left(\frac{a-b}{c} \right) \times 100 \right],$$

Where *a* is the mean optical density for the respective viral dilution, *b* is the mean optical density at the maximal cytopathic effect⁶, and *c* represents the mean optical density of uninfected cells (cell control). Viral titers are presented in logarithmic infectious units (logIU), measured as CCID50/0.1 mL.

Effect on viral replication

The antiviral activity of the NLC and HP-NLC samples was assessed by the virus-induced cytopathic effect inhibition assay in 96-well plates. Each well “received” 0.1 mL virus-containing material (100 CCID50). After one-hour adsorption, the unadsorbed virus was removed, and the corresponding nanosuspension was introduced into the wells⁷. The cells were incubated for 48 h at 37 °C and 5% CO₂. The cytopathic effect was determined by the neutral red uptake assay. To evaluate the antiviral activity of the nanosuspensions, the following control samples were also included: viral (inoculated with HSV-1) and toxicity control (containing only NLC/HP-NLC). The cytopathic effect

³ An adherent monolayer of Madin-Darby Bovine Kidney (MDBK) cell line (National Bank for Industrial Microorganisms and Cell Cultures, Sofia) was cultured in a DMEM medium supplemented with 10% fetal calf serum, 10 mM HEPES buffer, 100 IU/mL penicillin, and 100 µg/mL streptomycin. Incubation was carried out in a HERA cell 150 incubator at 37 °C and 5% CO₂ atmosphere.

⁴ The concentration at which the viability of 50% of the cell monolayer is affected due to the toxic effect of the test sample.

⁵ The highest concentration of the test sample that does not cause cell damage or death.

⁶ The control sample was obtained by inoculating cells with the maximally concentrated viral suspension.

⁷ Ten-fold descending dilutions of each lipid nanodispersion were previously prepared.

inhibition at each tested NLC/HP-NLC concentration was calculated according to the following equation:

$$\% \text{cytopathic effect} = \frac{\text{optical density}_{\text{test sample}} - \text{optical density}_{\text{viral control}}}{\text{optical density}_{\text{toxicity control}} - \text{optical density}_{\text{viral control}}} \times 100$$

The concentration of NLC/HP-NLC at which 50% inhibition of the cytopathic effect was observed compared to the viral control was defined as the inhibitory concentration 50%. The selectivity index of each lipid nanosuspension was calculated as the ratio of the cytotoxic concentration 50% and the inhibitory concentration 50%. The experiment was repeated acyclovir as a reference substance.

Virucidal activity

Samples with equal volumes of virus suspension (10^5 CCID₅₀/mL) and the corresponding NLC/HP-NLC sample at its maximum tolerated concentration were prepared and stored at room temperature for different intervals (15, 30, 60, 90, and 120 min). The residual infectious viral content was measured by the end-point dilution method⁸, and the viral titer in the samples was compared with a positive standard (ethanol 70%) and a viral control⁹ to calculate the viral load reductions (Δ logs).

Effect on viral adsorption

Pre-cooled 16-well plates (4 °C) were prepared, with each tested nanodispersion in its maximum tolerated concentration added to four wells, followed by a viral suspension (10^4 CCID₅₀). After one-hour incubation at 4 °C, the wells were washed with phosphate-buffered saline at different time intervals (15, 30, 45, and 60 min) to remove the nanosuspensions and unattached virus. The cells were then covered with maintenance medium and incubated at 37 °C for 24 h. The viral load in each sample was determined by the end-point dilution method after three freeze-thaw cycles⁵, compared to the viral control, and Δ log was calculated.

Antimicrobial activity

The antibacterial and antifungal activity of the NLC and HP-NLC samples was determined against *Escherichia coli* (ATCC 25922), *Staphylococcus aureus* (ATCC 25923), *Pseudomonas aeruginosa* (ATCC 10145), *Klebsiella pneumoniae* (ATCC 10031), and *Candida albicans* (ATCC 10231). Double-descending dilutions (from 1:2 to 1:256) of the nanosuspensions were made in 1.0 mL of Mueller-Hinton broth. Samples were inoculated with 0.1 mL microbial culture (standardized to 0.5 McFarland turbidity equivalent) and incubated under aerobic conditions for 24 h at 37 °C (bacterial strains) or for 48 h at 35 °C (*C. albicans*). Control samples included positive (obtained by mixing 0.1 mL of each microbial suspension with 1.0 mL of Mueller-Hinton broth) and negative (obtained by mixing the tested NLC/HP-NLC samples with Mueller-Hinton broth in a 1:1 ratio). The minimum bactericidal/fungicidal concentrations were determined by transferring a single-bacterial-loop volume of each sample onto blood agar and incubating under the conditions described above. The lowest concentration at which bacterial/fungal growth was inhibited at 99.9% was reported as the minimum bactericidal/fungicidal. All experiments were performed in triplicate.

3. Preparation and characterization of bigels

3.1. Preparation of bigels

The constituents of the biphasic gels, i.e., hydro- and oleogel, were prepared separately. The hydrogel was prepared by dissolving Poloxamer 407 (20%, w/w) in double-distilled water at 4 ± 1 °C for 24 h, then allowing it to form a gel structure at 25 ± 1 °C. The organogel was prepared by

⁸ Reed, L.J., Muench, H. (1938) 'A simple method of estimating fifty percent endpoints', American Journal of Hygiene, 27, 493-497.

⁹ The control contains equal volumes of virus suspension and maintenance medium.

dissolving sorbitan monostearate in borage oil (85:15 ratio) at 60 ± 2 °C under moderate stirring (200 rpm). To prepare the final bigel, the hot oleogel was added gradually to the hydrogel under continuous stirring at 1000 rpm for 10 min. Four “blank” bigels (BG) with different hydrogel-oleogel contents were obtained: BG1 (90:10), BG2 (80:20), BG3 (70:30), and BG4 (60:40). HP-NLC-containing bigels (HP-NLC-BG1, HP-NLC-BG2, HP-NLC-BG3, and HP-NLC-BG4) were prepared similarly, incorporating the selected HP-NLC dispersion into the hydrogel base before polymer dissolution and gelation. The extract concentration in the so-obtained bigels was 0.5% (w/w).

3.2. Characterization of bigels

Visual appearance

The color, odor, homogeneity, and consistency of the obtained bigels were evaluated organoleptically. The semi-solid structure formation was demonstrated by the tube inversion test¹⁰.

Morphological characteristics

The morphological features of the biphasic gels were examined using an optical microscope (Leica DM1000). An accurately weighed amount of each bigel was diluted with 10% aqueous methylene blue solution to a concentration of 0.5% (w/w) and ultrasonicated for 5 min to obtain homogeneous emulsions. Aliquots of each sample (10 μ L) were dripped onto a microscope slide and observed at 40x magnification. Images were captured using a camera (Leica ICC50W) and processed with Leica Application Suite software, version 3.4.0.

pH

The pH values of the semi-solid dosage forms were determined potentiometrically using a portable pH meter (pH 70 Vio). Each bigel was analyzed as a 10% (w/w) aqueous dispersion, with measurements taken in triplicate at 25 ± 1 °C.

Physical stability

The physical stability of the biphasic gels was tested using a D2012 Plus microcentrifuge at 25 ± 1 °C. Each sample (1.0 ± 0.1 g) was placed in a 2 mL centrifuge tube, and two consecutive centrifugation cycles were performed—at 4000 rpm for 10 min and at 5000 rpm for the same time¹¹.

Spreadability

The spreadability of the bigels was determined by the parallel plate method¹². 1.0 ± 0.1 g sample was pressed for 1 min between two glass plates, with the upper one weighing 125.0 g. The results, based on triplicate analysis, are presented in mm as the average spreading diameter.

Hardness, cohesiveness, and adhesiveness

The mechanical properties of the biphasic compositions were investigated with a texture analyzer (Belle) with an 18 mm cylindrical probe. The hardness, cohesiveness, and adhesiveness of the bigels were evaluated through a single compression test at a pre-set 5 kg load, with constant pre- and test speeds of 3 mm/s, and an insertion depth of 5 mm. The measurements were carried out thrice.

Rheological behavior

The rheological behavior of the bigels was determined using a viscometer (HAAKE™ Viscotester™ 550) at 20 ± 1 °C. Each sample was tested three times in a coaxial cylindrical sensor

¹⁰ Martín-Illana, A., Notario-Pérez, F., Cazorla-Luna, R., Ruiz-Caro, R., Bonferoni, M.C., Tamayo, A., Veiga, M.D. (2022) ‘Bigels as drug delivery systems: From their components to their applications’, *Drug Discovery Today*, 27(4), 1008-1026.

¹¹ Cervera-Khelifi, C., Saada, M., Hayouni, E.A., Tourette, A., Bouajila, J., Ksouri, R. (2020) ‘Development and Characterization of Novel Bigel-Based 1,4-Naphthoquinones for Topical Application with Antioxidant Potential’, *Arabian Journal of Science and Engineering*, 45(1), 53-61.

¹² Bashkurina, E.O., Anurova, M.O., Zavalniy, M.S., Demina, N.B., Bardakov, A.I., Krasnyuk I.I. (2022) ‘Dermatologic gels spreadability measuring methods comparative study’, *International Journal of Applied Pharmaceutics*, 14(1), 164-168.

SV DIN at shear rates ranging from 0.0123 to 1000 s⁻¹. Three different models were used to estimate the main rheological parameters (Table 1). Mathematical modelling was performed in the application software of the instrument—OS550.

Table 1. Mathematical models applied to calculate the rheological properties of bigels¹³.

Model	Mathematical equation
Bingham plastic model	$\tau = \tau_0 + \eta_p \times \gamma$
Power law model	$\tau = K \times \gamma^n$
Herschel-Bulkley model	$\tau = \tau_0 + K \times \gamma^n$

Note: τ , shear stress; γ , shear rate; τ_0 , yield stress; K , consistency index; n , power law index; η_p , plastic viscosity.

4. *In vivo* study of the wound healing potential of the prepared final semi-solid dosage form

A total of 119 male Wistar rats, aged approximately 100 days and weighing 200–250 g, were used. The animals, provided by the Vivarium at the Medical University of Varna, were reared individually under standard conditions (22 ± 1 °C, 55 ± 10% relative humidity, and 12-hour light/dark cycles) with free access to standard pelleted food and clean drinking water. Following a 10-day acclimatization, the experiments were conducted with approval from the Animal Ethics Committee of the Bulgarian Food Safety Agency (permit No. 265 of 02.06.2020) in compliance with Directive 2010/63/EU, the Basel Convention, and the Ethical Guidelines for Researchers of the International Council for Laboratory Animal Sciences.

Seven animals were used as a control group without excision wounds (Group 0; G0). The remaining ones were anesthetized with ketamine 5% and xylazine 2%, administered intramuscularly at a dose of 35.0 mg/kg and 5.0 mg/kg, respectively. After aseptic skin preparation, two full-thickness excision wounds (6 mm in diameter) were created on the upper back of each animal. The wounds were left open and cleaned daily with saline.

Animals were divided into groups of twenty-eight as follows:

- Group 1 (negative control group; G1)—untreated animals;
- Group 2 (positive control group; G2)—animals treated with a commercial product (cream) with a wound-healing effect¹⁴;
- Group 3 (experimental group; G3)—animals treated with a bigel comprising St. John’s wort extract rich in HP¹⁵;
- Group 4 (experimental group; G4)—animals treated with an HP-NLC-containing bigel.

4.1. Monitoring the wound-healing process

The wound healing was monitored in four intervals: two, seven, fourteen, and twenty-one days, with seven animals from each group included in each period. In groups 2, 3, and 4, the corresponding semi-solid form was applied topically once daily within the established research periods. Each wound area was photographed, and changes in wound size were monitored and compared.

4.2. Antioxidant status

The antioxidant status of the experimental animals was assessed at the end of each of the four wound-healing periods. After preliminary anesthesia with ketamine and xylazine, a blood sample was collected from the rat jugular vein, and the following analyses were performed:

¹³ Leusheva, E., Brovkina, N., Morenov, V. (2021) ‘Investigation of Non-Linear Rheological Characteristics of Barite-Free Drilling Fluids’, *Fluids*, 6, 327.

¹⁴ The semi-solid dosage form used contains extracts of aloe (*Aloe vera* (L.) Burm.f.), sweet almond (*Prunus amygdalus* Batsch), Chinese chaste tree (*Vitex negundo* L.), and Indian madder (*Rubia cordifolia* L.).

¹⁵ The bigel was prepared to assess the individual effects of HP compared to the other extract components. It was obtained by a similar methodology and contains 80% hydrogel and 20% oleogel. St. John’s wort extract (0.5%, w/w) was included in the oil base of the oleogel before gelation.

Antioxidant capacity

Plasma antioxidant capacity was determined using the ABTS (2,2'-azino-bis(3-ethylbenzothiazoline-6-sulfonic acid) method¹⁶ as follows: A specified volume of blood plasma (10 µL) was mixed with 1 mL of ABTS⁺ ¹⁷ solution in phosphate buffer with pH = 7.4. The absorbance of the resulting solution was determined immediately before and 6 min after the plasma was added, using a spectrophotometer (M501) at 734 nm. Phosphate buffer was used as a blank. The net absorbance (A) of each sample was calculated using the following equation:

$$A = [(A_{sample\ 0\ min} - A_{sample\ 6\ min}) - (A_{blank\ 0\ min} - A_{blank\ 6\ min})]$$

The quantitative analysis was conducted using the absolute calibration method, with uric acid as the standard. Plasma antioxidant capacity was reported as mmol/L uric acid equivalents (UAE). Each sample was analyzed in triplicate.

Degree of oxidative stress

The degree of oxidative stress was evaluated by measuring the plasma concentration of malondialdehyde (MDA)¹⁸. 100 µL plasma aliquots were mixed with 250 µL of trichloroacetic acid, and the resulting protein precipitate was removed. 150 µL of thiobarbituric acid was then added to the supernatant. The resulting samples were heated at 96 °C for 20 min, then cooled to room temperature. Their optical density was measured at 532 nm using a spectrophotometer, with thiobarbituric acid as the blank. For quantitative analysis, the external standard method was applied. Plasma MDA concentration was expressed in nmol/L as the average of three measurements.

Statistical data processing

Statistical analysis of the data was performed using SPSS software, version 26.0. The results were presented as mean ± standard deviation (SD). The differences between the means were assessed using analysis of variance (ANOVA) at a *p*-value of less than 0.05. Post-hoc comparisons were made using Duncan's test/Student's *t*-test.

¹⁶ Re, R., Pellegrini, N., Proteggente, A., Pannala, A., Yang, M., Rice-Evans, C. (1999) 'Antioxidant activity applying an improved ABTS radical cation decolorization assay', *Free Radical Biology and Medicine*, 26(9-10), 1231-1237.

¹⁷ The monocation was obtained via a reaction between the diammonium salt of 2,2'-azino-bis(3-ethylbenzothiazoline-6-sulfonic acid) and potassium persulfate.

¹⁸ Porter, N.A., Nixon, J., Isaac, R. (1976) 'Cyclic peroxides and the thiobarbituric assay', *Biochimica et Biophysica Acta – Lipids and Lipid Metabolism*, 441(3), 506-512.

IV. Results and discussion

1. Preparation and chromatographic analysis of hyperforin-rich St. John's wort extract

The experimental setup utilized in isolating St. John's wort extract with a high HP content is presented in Figure 1. The maceration method was applied due to HP's thermolability and was further modified according to its photoinstability and reactivity toward oxygen. The extraction was carried out in the dark in a borosilicate amber glass flask, and the maceration medium was purged with argon purging was performed to remove the atmospheric O₂. The resulting after 48-h maceration, filtration, and organic solvent removal extracts are thick, viscous, dark green masses.

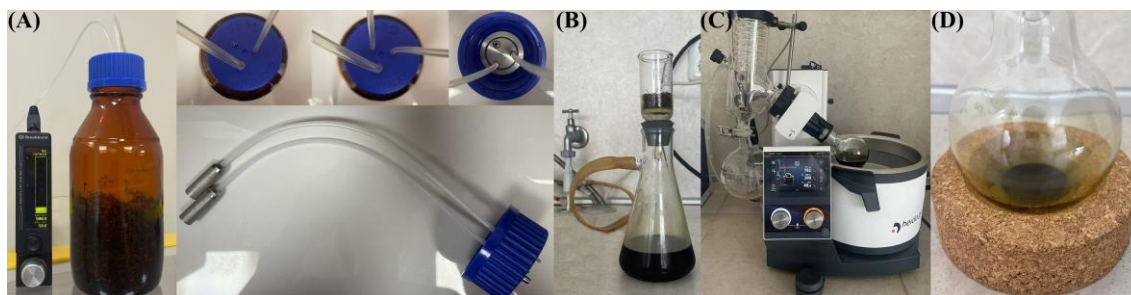


Figure 1. Experimental setup used to obtain an HP-rich St. John's wort extract. The "maceration vessel" is presented in subfigure (A), while the setups used for vacuum filtration of the macerate and removal of the solvent under reduced pressure are shown in subfigures (B) and (C), respectively. The final product (HP-rich St. John's wort extract) is given in subfigure (D).

For the qualitative and quantitative analysis of HP in the obtained St. John's wort extracts, a validated HPLC-UV protocol¹ was employed. A high concentration of HP was found in both maceration-obtained extracts (> 5.0 µg/mL; Figure 3 (B) and (C)). The presented chromatograms also show the impact of the solvent-to-solid ratio: increasing the amount of extractant led to a higher concentration of the desired phloroglucinol—from 5.30 to 8.87 µg/mL. With a plant material-to-extractant ratio of 1:3.33, the extract quality was comparable to that of a commercial supercritical CO₂ extract with high HP content (40.1%) (Figure 3 (A) and (B)). For this reason, it was selected for further experimental work.

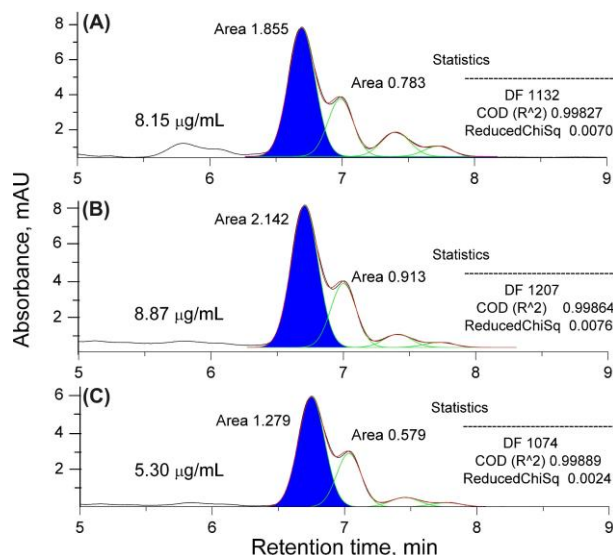


Figure 2. Comparative HPLC analysis of a commercial St. John's wort extract rich in HP (A), an extract obtained by maceration at a solvent-to-solid ratio of 1:3.33 (B), and an extract obtained by maceration at a solvent-to-solid ratio of 1:2.5 (C). The complex-composition chromatographic peaks are deconvoluted and presented in green, and the area of the significant (HP) peaks is filled in blue. The superpositions of the green-colored bands are presented in red. The degrees of coincidence of the latter with the real chromatograms were statistically evaluated and the results obtained are presented in each subfigure.

2. Development and characterization of nanostructured lipid carriers loaded with hyperforin-rich St. John's wort extract

2.1. Development of "blank" nanostructured lipid carriers by high-shear homogenization with subsequent ultrasonication while varying solid lipids, liquid oils, and experimental conditions

To evaluate the influence of composition and experimental conditions on the characteristics of the obtained "blank" nanoparticles, twenty different models were developed (Table 2).

Table 2. Composition of NLC samples and experimental conditions applied during their preparation.

Sample	Lipid phase, 10% (w/w)				Surfactants, 5% (w/w)		Aqueous phase, 85% (w/w)	Homogenization speed, rpm	Ultrasonication duration, min	Ultrasonication temperature, °C
	Solid lipid (% w/w)		Liquid lipid (% w/w)		SMO (% w/w)	PSMO (% w/w)	Double-distilled water (% w/w)			
	BW	GB	AO	BO						
NLC1	7		3		2	3	85	10 000	15	25 ± 1
NLC2	7			3	2	3	85	10 000	15	25 ± 1
NLC3		7	3		2	3	85	10 000	15	25 ± 1
NLC4		7		3	2	3	85	10 000	15	25 ± 1
NLC5	7		3		2	3	85	10 000	15	4 ± 1
NLC6	7			3	2	3	85	10 000	15	4 ± 1
NLC7		7	3		2	3	85	10 000	15	4 ± 1
NLC8		7		3	2	3	85	10 000	15	4 ± 1
NLC9	7		3		2	3	85	10 000	5	25 ± 1
NLC10	7			3	2	3	85	10 000	5	25 ± 1
NLC11		7	3		2	3	85	10 000	5	25 ± 1
NLC12		7		3	2	3	85	10 000	5	25 ± 1
NLC13	7		3		2	3	85	10 000	5	4 ± 1
NLC14	7			3	2	3	85	10 000	5	4 ± 1
NLC15		7	3		2	3	85	10 000	5	4 ± 1
NLC16		7		3	2	3	85	10 000	5	4 ± 1
NLC17	7		3		2	3	85	15 000	-	-
NLC18	7			3	2	3	85	15 000	-	-
NLC19		7	3		2	3	85	15 000	-	-
NLC20		7		3	2	3	85	15 000	-	-

2.2. Characterization of the "blank" nanostructured lipid carriers

Visual appearance

All obtained nanodispersions were white, milky liquids. Samples prepared at a higher homogenization speed (15,000 rpm) showed a significant amount of foam, which may potentially lead to physical instability of the NLC dispersions. For this reason, lipid nanosuspensions prepared at 15,000 rpm were excluded from the study.

Mean particle size, particle size distribution, and zeta potential

The influence of the experimental conditions (duration and temperature of ultrasonication) on the average particle size, particle size distribution, and zeta potential was considered, and only the duration of the ultrasonic application was proven to impact them. Shorter ultrasonication resulted in

larger particles, a more heterogeneous particle size distribution, and higher absolute zeta potential values (Figure 3).

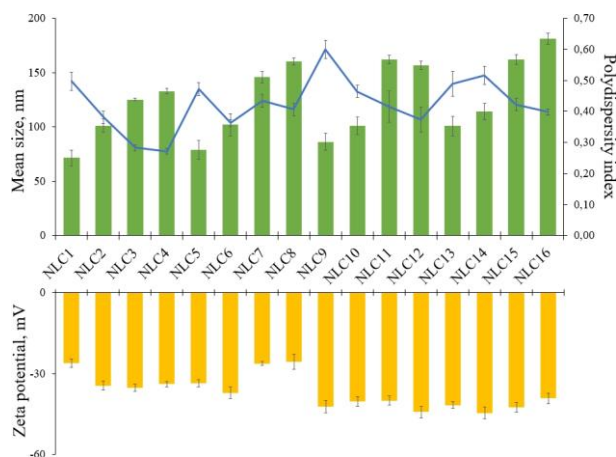


Figure 3. Mean particle size, polydispersity index, and zeta potential of NLC samples. The diagram shows the averaged results from triplicate measurements and SD.

The results of the study on mean particle size, polydispersity index, and zeta potential showed that shorter ultrasonication resulted in lipid dispersions with larger particles and a multimodal size distribution. Therefore, eight of the samples (NLC9–NLC16) were excluded from the study.

Degree of crystallinity

The characteristic reflections of BW and GB (at scattering angles $2\theta = 2.62, 19.56, 21.74,$ and 24.14° for BW and at $2\theta = 4.31, 21.74,$ and 24.14° for GB, respectively) are observed in the X-ray diffraction patterns of the lipid melts and NLC samples, with identical d-spacing values, indicating no polymorphic transformations during the experiments. The addition of a liquid lipid reduces the crystallinity of solid lipids, with a noticeable decrease in both lipid melts. This effect is only observed in GB-containing nanoparticles, suggesting a “more disordered” structure. Additionally, no significant difference was found between the diffractograms of samples NLC3 and NLC7, or between NLC4 and NLC8, indicating the changes in the ultrasonication temperature do not cause polymorphic transitions (Figure 4).

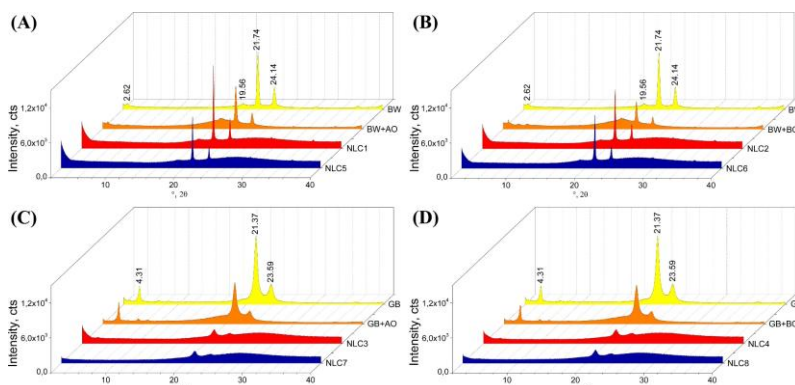


Figure 4. X-ray diffraction patterns of solid lipids (BW and GB), lipid melts of solid and liquid lipid (BW+AO, BW+BO, GB+AO, and GB+BO), and NLC suspensions (NLC1–NLC8). The samples are distributed in the subfigures according to the type of lipids used: BW and AO (A); BW and BO (B); GB and AO (C); GB and BO (D). The area under the curve in the X-ray diffraction patterns of the different analytes is colored as follows: solid lipids—yellow; lipid melts—orange; NLC carriers obtained at 25 °C—red; NLC samples obtained at 4 °C—blue.

Physical stability during storage

BW-containing samples showed phase separation after one month of storage at 4 °C and gelation after six months under the same conditions (Figure 5). Due to concerns about physical instability, BW-based NLC samples were excluded from the study.



Figure 5. Visual appearance of NLC dispersions immediately after preparation (A) and after one month of storage at 4 °C (B). Gelation in BW-based systems is presented in subfigure (C).

Based on the results obtained, only two of the initially set samples were determined as optimal, viz., NLC3 and NLC4. Additional analyses after loading with the selected extract were conducted only with them.

2.3. Characterization of the nanocarriers loaded with hyperforin-rich St. John’s wort extract

Visual appearance

Immediately after their preparation, the HP-rich St. John’s wort extract-loaded nanodispersions (HP-NLCs) were stored in dark glass vials. Both prepared HP-NLC samples retained the characteristic green color of the extract. The physical stability of the nanodispersions was monitored visually over one year of storage at 4 °C. They maintained their original appearance and showed no macroscopic signs of physical instability.

Mean particle size, particle size distribution, and zeta potential

The average particle size, particle size distribution, and zeta potential were monitored over a one-year period. Measurements were taken immediately after preparation, and then at one, six, and twelve months of storage at 4 °C (Table 3).

Table 3. Mean particle size, polydispersity index, and zeta potential of extract-loaded NLC systems (HP-NLCs). The values presented in the table are the means from triplicate measurements \pm SD.

Sample	Day	Mean size, nm	Polydispersity index	Zeta potential, mV
HP-NLC3	0	142.97 \pm 2.00 ^c	0.25 \pm 0.01 ^d	-36.53 \pm 3.02 ^{a,b}
	30	212.17 \pm 2.76 ^a	0.43 \pm 0.02 ^a	-39.55 \pm 3.24 ^{a,b,c}
	180	206.93 \pm 4.18 ^a	0.45 \pm 0.02 ^a	-39.96 \pm 1.67 ^{b,c}
	365	209.37 \pm 3.32 ^a	0.44 \pm 0.01 ^a	-43.10 \pm 1.20 ^c
HP-NLC4	0	146.00 \pm 3.24 ^c	0.28 \pm 0.02 ^c	-36.22 \pm 1.68 ^a
	30	181.13 \pm 3.65 ^b	0.34 \pm 0.03 ^b	-42.22 \pm 1.36 ^c
	180	180.17 \pm 1.00 ^b	0.31 \pm 0.03 ^{b,c}	-39.93 \pm 0.65 ^{b,c}
	365	174.50 \pm 6.52 ^b	0.29 \pm 0.01 ^c	-38.09 \pm 0.81 ^{a,b}

Mean values in each column marked with the same indices are statistically indistinguishable ($p < 0.05$).

The average particle size in both samples is within the nano-range, below 250 nm (Table 3). Over time, the particle sizes in both samples gradually increase, with a more noticeable rise in the average diameter of the HP-NLC3 carriers. Both nanodispersions showed a homogeneous particle size distribution, with polydispersity indices below 0.5. While HP-NLC3 initially had a lower polydispersity index, it increased after one month of storage, whereas HP-NLC4 maintained a significantly lower polydispersity throughout the one-year period, except on day 0. As to zeta potential, the particles of the studied lipid nanosuspensions possessed values higher than |30 mV| (Table 3), remaining high throughout the one-year storage period and indicating good physical stability.

Shape and inner morphology

The TEM results of all four samples (HP-NLC3, HP-NLC4, and their “blank” counterparts) confirm the reported average hydrodynamic diameter of the particles (Figure 6). The micrographs of all samples reveal mostly irregularly shaped particles with a well-defined core and shell. All four systems can be attributed to NLC with an imperfect crystalline matrix. In the presence of the plant extract, the bilayer structure of the nanocarriers appears more amorphous, but the encapsulation does not affect the matrix organization or integrity.

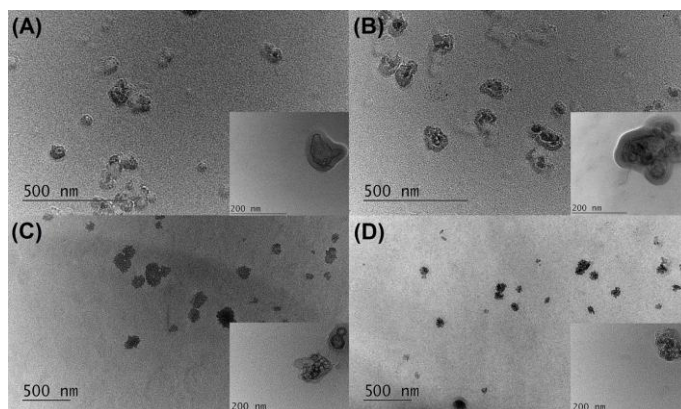


Figure 6. TEM images of NLC3 (A), HP-NLC3 (B), NLC4 (C), and HP-NLC4 (D).

Degree of crystallinity

The diffractograms of extract-loaded nanoparticles show the characteristic reflections of the solid lipid, though with significantly lower intensity compared to GB and NLC samples (Figure 7), demonstrating that incorporating the extract in the nanocarriers reduces the solid lipid’s degree of crystallinity. This argument is supported by the data obtained from the TEM analysis. The β' crystal structure of the used glyceride is retained in HP-NLC dispersions, with no evidence of polymorphic changes, indicating no rapid expulsion of the included extract from the nanocarriers is to be expected. The diffractogram of the St. John’s wort extract shows two reflections at 21.80 and 29.65°, which are absent in the HP-NLCs diffractograms, suggesting the extract is in amorphous or molecularly dispersed state within the lipid matrix of the nanoparticles.

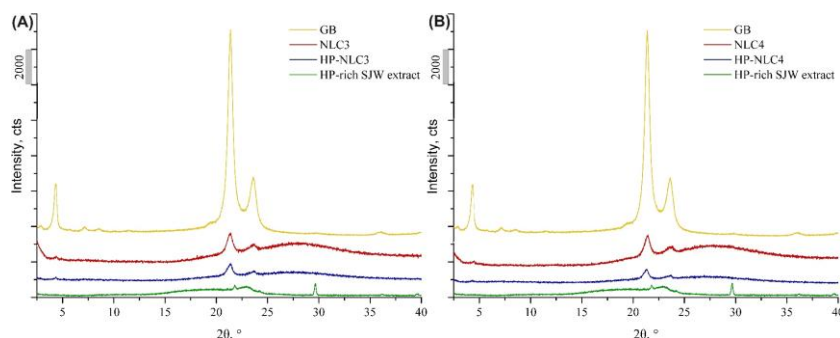


Figure 7. X-ray diffraction patterns of GB, “blank” nanoparticles (NLC3 and NLC4), extract-loaded nanocarriers (HP-NLC3 and HP-NLC4), and HP-rich St. John’s wort extract (HP-rich SJW extract). The samples are divided into two subfigures according to the type of oil used: AO (A) and BO (B). The analyte bands are colored as follows: GB—yellow; NLC dispersions—red; HP-NLC systems—blue; HP-rich St. John’s wort extract—green.

Entrapment efficiency

Both samples demonstrate successful encapsulation of the extract, as indicated by the relatively high HP content in them (> 70% of the initial content) (Table 4). Given the pronounced chemical instability of phloroglucinol, it is expected that its amount in the nanocarriers decreases during their storage. Notably, HP-NLC4 demonstrated higher EE and superior stabilization of the HP-rich extract over time.

Table 4. Entrapment efficiency of HP-NLC dispersions. Mean values from triplicate analyses \pm SD are presented.

Day	HP-NLC3	HP-NLC4
0	70.44 \pm 0.21 ^c	74.49 \pm 0.23 ^a
30	65.61 \pm 0.20 ^d	72.10 \pm 0.25 ^b
180	50.55 \pm 0.18 ^g	63.51 \pm 0.23 ^e
365	41.82 \pm 0.61 ^h	53.47 \pm 0.62 ^f

Mean values marked with different letter indices are statistically distinguishable ($p < 0.05$).

Extract-lipid interactions

The successful encapsulation of the HP-rich St. John's wort extract is evident from the infrared spectra of HP-NLC3 and HP-NLC4 (1.25%), which exhibit the characteristic features of both "blank" nanoparticles and extract (Figure 8). Notably, the C=C vibration region (from 1600 to 1630 cm^{-1}) reveals an absorption band at 1623 cm^{-1} , which intensifies proportionally with higher extract concentrations (2.50 and 5.00%). Additionally, an absorption band at 1600 cm^{-1} , characteristic of the extract itself, emerges in overloaded samples, indicating the co-aggregate formation between the extract and the HP-NLC particles.

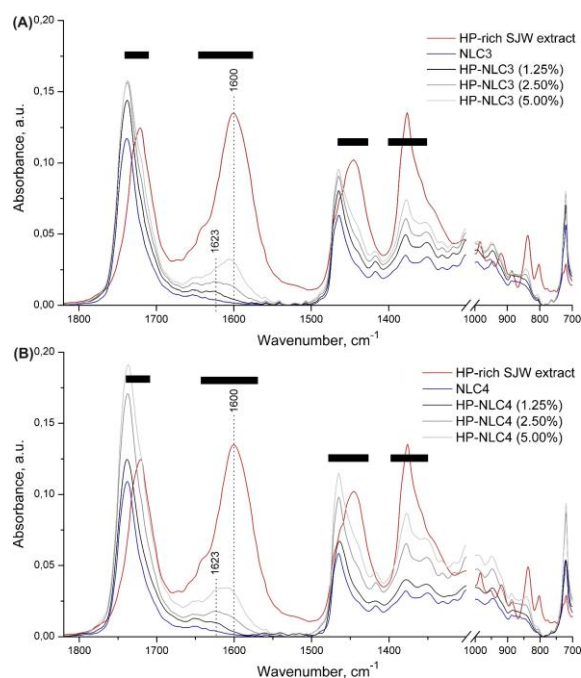


Figure 8. Infrared spectra of HP-rich St. John's wort extract (HP-rich SJW extract; red band), "blank" (NLC3 and NLC4; blue band), and extract-loaded lipid nanocarriers (HP-NLC3 and HP-NLC4; represented by bands colored in different shades of the gray scale according to the quantity of the extract in them). The spectra of the samples are divided into two subfigures according to the type of liquid lipid contained in them: AO (A) and BO (B).

Antiviral activity

The "blank" NLC samples exhibited no toxicity even at the highest tested concentrations. In contrast, the nanocarriers containing the extract displayed higher cytotoxicity than acyclovir, though HP-NLC4 demonstrated lower MDBK toxicity—approximately 2.5 times higher than the reference substance (Table 5).

Table 5. Cytotoxicity of the tested HP-NLC samples. Concentrations are expressed relative to the plant extract.

Sample	Cytotoxic concentration 50% ($\mu\text{g/mL}$)	Maximum tolerated concentration ($\mu\text{g/mL}$)	Inhibitory concentration 50% ($\mu\text{g/ml}$)	Selectivity index
HP-NLC3	87.50 \pm 2.30*	12.50	25.30 \pm 2.20**	3.46
HP-NLC4	94.70 \pm 3.60*	12.50	23.70 \pm 2.10**	4.00
Acyclovir	291.00 \pm 9.40	-	0.33 \pm 0.03	881.82

The asterisks indicate a statistically significant difference with the data from the analysis of the reference substance. The level of statistical significance is reflected by the number of asterisks—one ($p < 0.05$) or ($p < 0.001$).

Within the non-toxic concentration range, the “blank” nanoparticles showed no impact on HSV-1 replication, while HP-NLC nanodispersions exhibited significantly weaker activity compared to acyclovir (Table 5). Among the tested formulations, HP-NLC4 demonstrated the most notable effect, indicated by a higher selectivity index.

HP-NLC3 and HP-NLC4 also had no impact on extracellular HSV-1 virions within 120 min (Table 6), confirming the absence of a virucidal effect and suggesting that the nanoparticles function solely as carriers without releasing the extract (or HP) outside the cell.

Table 6. Virucidal effect of the studied nanocarriers against HSV-1.

Sample	$\Delta\log$				
	15 min	30 min	45 min	60 min	120 min
NLC3	0.50	0.50	0.50	0.50	0.50
HP-NLC3	1.00	1.00	1.00	1.00	1.00
NLC4	0.50	0.50	0.50	0.50	0.50
HP-NLC4	0.50	0.50	0.75	0.75	0.75
Ethanol 70%	8.00	8.00	8.00	8.00	7.75

The most pronounced effect on viral adsorption (reduction in viral load), yet still insignificant, occurred after 1 h exposure to HP-NLC4 (Table 7). The absence of significant changes in viral titers suggests that none of the tested samples influence the interaction between viral structures and cell membranes, and confirms that the lipid nanoparticles serve solely as extract carriers.

Table 7. Effect of NLC and HP-NLC dispersions on the initial stage of the HSV-1 life cycle.

Sample	$\Delta\log$			
	15 min	30 min	45 min	60 min
NLC3	0.25	0.25	0.25	0.50
HP-NLC3	0.25	0.25	0.50	0.50
NLC4	0.00	0.25	0.25	0.50
HP-NLC4	0.25	0.25	0.50	0.75

Antimicrobial activity

After dilution, inoculation, and incubation, all test samples appeared opaque, similar to the NLC/HP-NLC dispersions and the negative controls, which made it impossible to visually assess the minimum inhibitory concentrations based on turbidity. Therefore, only the minimum bactericidal and fungicidal concentrations of each nanosuspension were determined. The “blank” nanocarriers showed no activity against the target pathogens (Figure 9).

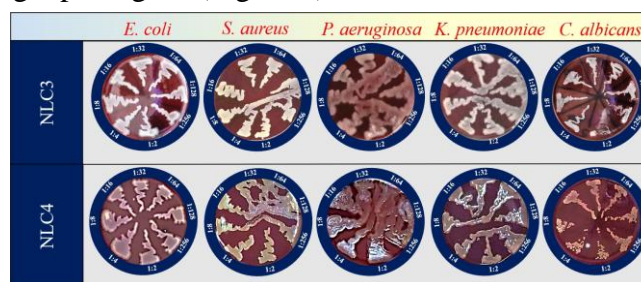


Figure 9. Antibacterial and antifungal activity of NLC3 and NLC4.

Both extract-loaded nanodispersions demonstrated antimicrobial activity against the specified pathogens, with HP-NLC4 showing a significantly stronger effect (Figure 10). For HP-NLC4, the minimum bactericidal concentration against *K. pneumoniae* was 0.0977 mg/mL (dilution 1:128), and the minimum fungicidal concentration was approximately 0.0488 mg/mL (dilution 1:256). A weaker yet noticeable activity was observed against *S. aureus*, with a minimum bactericidal concentration of 6.25 mg/mL (dilution 1:2). Both HP-NLC samples showed no activity against Gram-negative *E. coli*

and *P. aeruginosa*. These results indicate that the antimicrobial activity of the HP-NLC samples is entirely attributed to the extract they contain, not to any of their structural components.

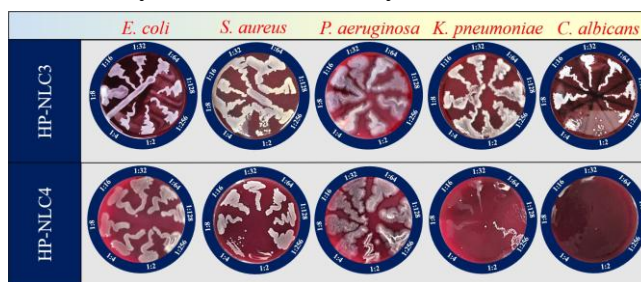


Figure 10. Antibacterial and antifungal activity of HP-NLC3 and HP-NLC4.

Based on the obtained data, HP-NLC4 was selected as the preferred carrier for the HP-rich St. John's wort extract. The low viscosity of the nanodispersion necessitated its incorporation into a semi-solid vehicle prior to topical administration. For this purpose, eight biphasic gels (bigels)—“blank” and loaded with HP-NLC4, were prepared and characterized.

3. Development and characterization of a semi-solid dosage form (biphasic gel) incorporating nanostructured lipid carriers loaded with hyperforin-rich St. John's wort extract

Visual appearance

All “blank” formulations are white, semisolid masses, while the HP-NLC4-loaded semisolid forms display the pale green color of the nanodispersion (Figure 11). The tube inversion test showed that the bigels have sufficient structural stability and yield strength, as they did not flow when inverted. The bigels containing 40% oil phase (BG4 and HP-NLC-BG4) had a greasy consistency due to their higher oleogel content, and further studies were not conducted on them.

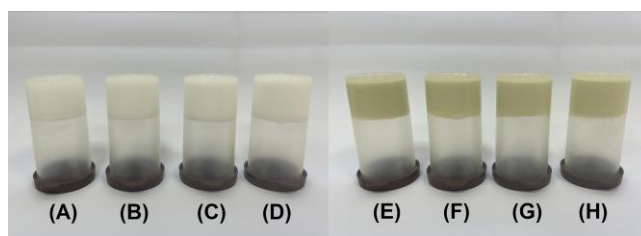


Figure 11. Visual appearance of BG1 (A), BG2 (B), BG3 (C), BG4 (D), HP-NLC-BG1 (E), HP-NLC-BG2 (F), HP-NLC-BG3 (G), and HP-NLC-BG4 (H).

Morphological characteristics

In BG1 and BG3, the oleogel phase is unevenly distributed, with some exceeding 5 μm in diameter. In contrast, BG2 shows a higher degree of uniformity. For the HP-NLC4-containing semi-solid forms, the composition with a 20% oil phase is again more homogeneous. Similar to the “blank” bigels, oleogel aggregates are also present in HP-NLC-BG1 and HP-NLC-BG3 (Figure 12).

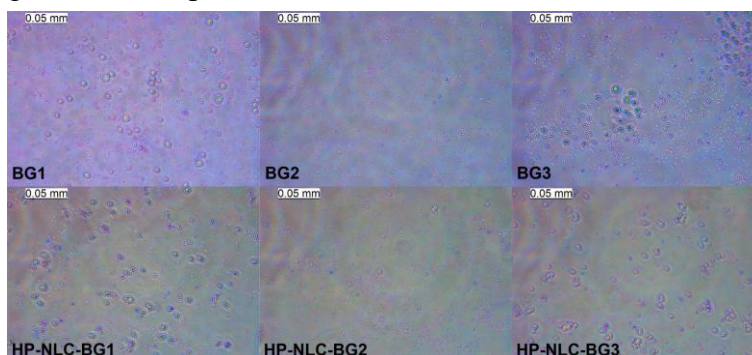


Figure 12. Micrographs of “blank” and HP-NLC4-loaded bigels.

pH

The pH values of the semi-solid carriers ranged from 6.04 ± 0.01 to 6.82 ± 0.05 (Table 8). The inclusion of the nanodispersion resulted in a significant increase in acidity, but all semi-solid formulations maintained pH values close to those physiologically tolerated by the skin. Therefore, none of the bigels is expected to cause irritation upon application.

Table 8. pH values of the studied bigels. The table presents the average values of three measurements \pm SD.

Sample	pH value
BG1	6.79 ± 0.07^a
BG2	6.81 ± 0.05^a
BG3	6.82 ± 0.01^a
HP-NLC-BG1	6.05 ± 0.01^b
HP-NLC-BG2	6.04 ± 0.01^b
HP-NLC-BG3	6.05 ± 0.03^b

Mean values marked with the same letter indices are statistically indistinguishable ($p < 0.05$).

Physical stability

None of the compositions exhibited phase separation under the applied centrifugal force (4000 rpm for 10 min and 5000 rpm for the same time) (Figure 13). They maintained their structural integrity, confirming their physical stability.

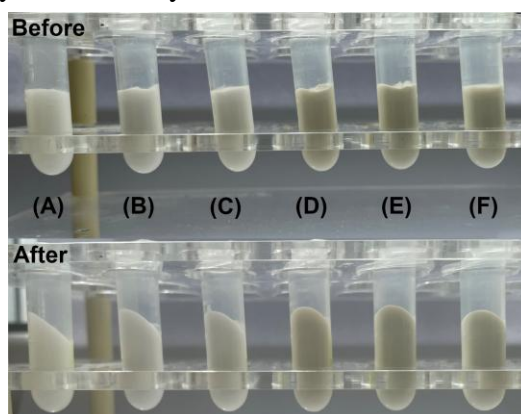


Figure 13. Visual appearance of BG1 (A), BG2 (B), BG3 (C), HP-NLC-BG1 (D), HP-NLC-BG2 (E), and HP-NLC-BG3 (F) before and after centrifugation.

Mechanical properties

The results of the mechanical tests performed are presented in Table 9.

Table 9. Mechanical properties of the prepared bars. The table shows the average values of the corresponding parameters \pm SD from triplicate measurements.

Sample	Spreadability, mm	Hardness, g	Cohesiveness, g.s	Adhesiveness, g.s
BG1	31.50 ± 0.89^a	71.07 ± 0.09^e	86.27 ± 1.25^d	-14.17 ± 0.63^a
BG2	$30.17 \pm 0.42^{a,b}$	74.67 ± 0.94^e	90.37 ± 1.20^d	-16.03 ± 0.31^a
BG3	$29.00 \pm 0.41^{b,c}$	81.00 ± 2.94^d	93.70 ± 3.77^d	-15.13 ± 1.03^a
HP-NLC-BG1	$28.17 \pm 0.12^{c,d}$	112.33 ± 4.71^c	138.80 ± 9.01^c	-19.37 ± 0.90^b
HP-NLC-BG2	26.83 ± 0.96^d	137.33 ± 3.77^b	167.60 ± 8.71^b	-25.10 ± 0.37^c
HP-NLC-BG3	24.75 ± 1.08^e	148.03 ± 0.08^a	182.63 ± 0.70^a	-25.17 ± 1.35^c

There is a statistically significant difference ($p < 0.05$) between the mean values marked with different letter indices in each column.

According to Lardy et al.'s classification that considers the spreading diameter of gels, the prepared bigels can be identified as very stiff ($\varnothing \leq 40$ mm)¹⁹ (Table 9). All HP-NLC4-containing semi-solid dosage forms spread less than their corresponding "blank" formulations. The statistically

¹⁹ Depending on the spreading diameter (\varnothing , mm), semi-solid forms can be classified as fluid ($\varnothing > 70$ mm), semi-fluid ($70 \geq \varnothing > 55$ mm), semi-stiff ($55 \geq \varnothing > 47$ mm), stiff ($47 \geq \varnothing > 40$ mm), and very stiff ($\varnothing \leq 40$ mm).

Lardy, F., Vennat, B., Pouget, M.P., Pourrat, A. (2000) 'Functionalization of hydrocolloids: Principal component analysis applied to the study of correlations between parameters describing the consistency of hydrogels', Drug Development and Industrial Pharmacy, 26, 715-721.

significant difference in spreading diameters of BG1 and BG3, as well as between their loaded counterparts consider the 20% oleogel content as a threshold beyond which spreadability significantly decreases.

All three bigels loaded with HP-NLC4 exhibited significantly higher hardness than the “blank” ones (Table 9, Figure 14). Regarding the hydrogel-to-oleogel ratio, a significant change in the studied parameter was observed only in the “blank” sample with a 30% oil phase content. In the loaded bigels, a gradual increase in hardness was noted with the rising percentage of oleogel content.

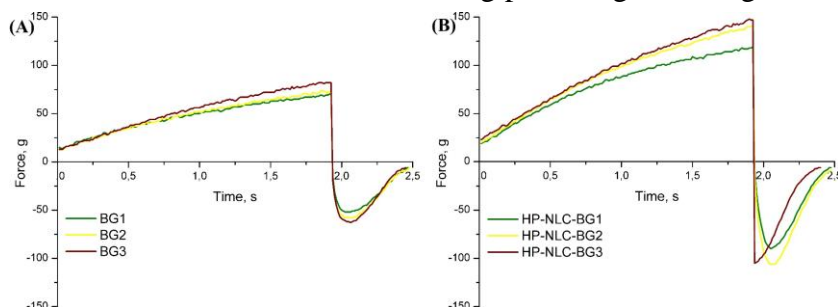


Figure 14. Graphically presented force-time relationship derived using a single compression test. Subfigure (A) shows the texture profiles of the “blank” and (B)—those of the HP-NLC4-loaded bars.

The cohesiveness of the HP-NLC4-containing formulations was significantly higher than that of their “blank” counterparts. However, the increase in the oleogel content leads to a significant change in the studied parameter only in the nanodispersion-loaded bigels.

As to adhesiveness, the inclusion of the lipid nanodispersion in the bigels impacted this parameter significantly. The three “blank” semi-solid dosage forms showed similar values of this parameter, but the addition of HP-NLC4 led to its pronounced increase. The differences in the adhesiveness between HP-NLC-BG1 and HP-NLC-BG3 are attributed to the hydrogel-to-oleogel ratio—20% lipophilic phase led to the most adhesive bigels, with no significant changes observed as its percentage increases.

Rheological behavior

The data from the rheological analyses of the “blank” bigels are presented in Table 11.

Table 10. Rheological parameters of the “blank” bigels calculated using different mathematical models. The table shows the average values from triplicate measurements \pm SD.

Mathematical model	BG1	BG2	BG3
Bingham plastic model	$\eta_p = 0.57 \pm 0.04 \text{ Pa}\cdot\text{s}$ $\tau_0 = 354.89 \pm 9.1 \text{ Pa}$ $R^2 = 0.84$	$\eta_p = 0.30 \pm 0.09 \text{ Pa}\cdot\text{s}$ $\tau_0 = 440.44 \pm 22.92 \text{ Pa}$ $R^2 = 0.17$	$\eta_p = 0.77 \pm 0.06 \text{ Pa}\cdot\text{s}$ $\tau_0 = 365.43 \pm 12.28 \text{ Pa}$ $R^2 = 0.78$
Power law model	$K = 322.63 \pm 0.1 \text{ Pa}\cdot\text{s}^n$ $n = 0.11 \pm 0.01$ $R^2 = 0.88$	$K = 394.62 \pm 17.45 \text{ Pa}\cdot\text{s}^n$ $n = 0.08 \pm 0.01$ $R^2 = 0.72$	$K = 328.76 \pm 6.02 \text{ Pa}\cdot\text{s}^n$ $n = 0.12 \pm 0.01$ $R^2 = 0.96$
Herschel-Bulkley model	$\tau_0 = 283.59 \pm 4.41 \text{ Pa}$ $K = 37.12 \pm 3.25 \text{ Pa}\cdot\text{s}^n$ $n = 0.38 \pm 0.01$ $R^2 = 0.99$	$\tau_0 = 0 \pm 0.01 \text{ Pa}$ $K = 394.72 \pm 48.4 \text{ Pa}\cdot\text{s}^n$ $n = 0.08 \pm 0.01$ $R^2 = 0.60$	$\tau_0 = 236.02 \pm 8.64 \text{ Pa}$ $K = 88.59 \pm 7.99 \text{ Pa}\cdot\text{s}^n$ $n = 0.28 \pm 0.01$ $R^2 = 0.99$

Note: τ , shear stress; $\dot{\gamma}$, shear rate; τ_0 , yield stress; K , consistency index; n , power law index; η_p , plastic viscosity.

The flow properties of BG1 and BG3 are best described by the Herschel-Bulkley model, as indicated by the coefficient of determination $R^2 = 0.99$ (Table 10). BG1 and BG3 have flow indices less than unity, indicating that they exhibit pseudoplastic properties. This rheological behavior is further confirmed by the relationship between dynamic viscosity and applied shear rate (Figure 15).

Despite the relatively low coefficient of determination, $R^2 = 0.72$, the Power law model best reflects the rheological behavior of BG2. The bigel in question also exhibits pseudoplastic properties with a flow index less than unity.

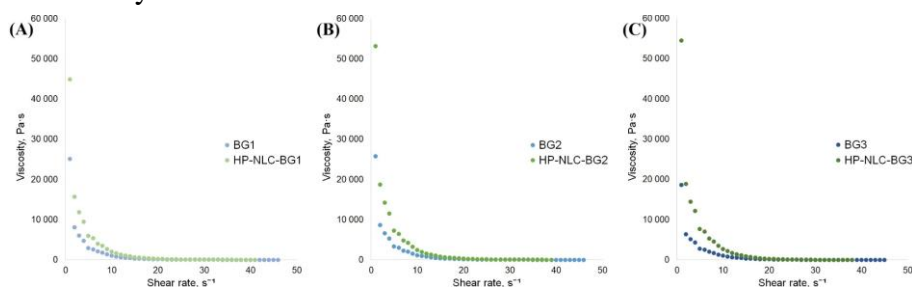


Figure 15. Relationship between shear rate and viscosity of BG1 and HP-NLC-BG1 (A), BG2 and HP-NLC-BG2 (B), and BG3 and HP-NLC-BG3 (C).

The rheological properties of HP-NLC4-containing bigels are best described by the Herschel-Bulkley model (Table 11), classifying them as pseudoplastic non-Newtonian systems. This is evident by their low n -values and the shear rate dependence on the dynamic viscosity (Table 11, Figure 15). Among the studied bigels, HP-NLC-BG2 exhibits the lowest flow index and the highest consistency coefficient, showing the most pronounced pseudoplastic behavior. As a result, HP-NLC-BG2 is expected to have the most desirable texture among all nanodispersion-loaded bigels.

Table 11. Rheological parameters of HP-NLC4-loaded bigels calculated using different mathematical models. The table presents the average values \pm SD from triplicate measurements.

Mathematical model	HP-NLC-BG1	HP-NLC-BG2	HP-NLC-BG3
Bingham plastic model	$\eta_p = 2.22 \pm 0.01 \text{ Pa}\cdot\text{s}$ $\tau_0 = 627.68 \pm 8.32 \text{ Pa}$ $R^2 = 0.93$	$\eta_p = 2.61 \pm 0.17 \text{ Pa}\cdot\text{s}$ $\tau_0 = 758.79 \pm 9.49 \text{ Pa}$ $R^2 = 0.86$	$\eta_p = 3.05 \pm 0.15 \text{ Pa}\cdot\text{s}$ $\tau_0 = 778.84 \pm 6.57 \text{ Pa}$ $R^2 = 0.92$
Power law model	$K = 627.79 \pm 14.58 \text{ Pa}\cdot\text{s}^n$ $n = 0.11 \pm 0.01$ $R^2 = 0.88$	$K = 768.86 \pm 8.86 \text{ Pa}\cdot\text{s}^n$ $n = 0.06 \pm 0.01$ $R^2 = 0.87$	$K = 768.89 \pm 8.86 \text{ Pa}\cdot\text{s}^n$ $n = 0.06 \pm 0.01$ $R^2 = 0.87$
Herschel-Bulkley model	$\tau_0 = 578.53 \pm 2.53 \text{ Pa}$ $K = 27.09 \pm 1.52 \text{ Pa}\cdot\text{s}^n$ $n = 0.55 \pm 0.01$ $R^2 = 0.99$	$\tau_0 = 682.31 \pm 5.41 \text{ Pa}$ $K = 59.90 \pm 4.94 \text{ Pa}\cdot\text{s}^n$ $n = 0.40 \pm 0.02$ $R^2 = 0.99$	$\tau_0 = 762.52 \pm 8.15 \text{ Pa}$ $K = 11.35 \pm 3.77 \text{ Pa}\cdot\text{s}^n$ $n = 0.73 \pm 0.07$ $R^2 = 0.94$

Note: τ , shear stress; $\dot{\gamma}$, shear rate; τ_0 , yield stress; K , consistency index; n , power law index; η_p , plastic viscosity.

Taking into account all the conducted studies and conclusions, HP-NLC-BG2 was chosen as the carrier for the nanoencapsulated HP-rich St. John's wort extract. The final step is in vivo testing of its wound healing and antioxidant properties on experimental animals.

4. **In vivo study of the wound-healing potential of the prepared final semi-solid dosage form on an excision wound model in experimental animals**

4.1. **Monitoring the dynamics of tissue repair based on changes in the wound size over time**

The wound-healing dynamics were monitored visually, as wound areas were photographed on pre-selected post-excision days (Figure 16). The photographs demonstrate complete wound healing in all studied groups by day twenty-one. However, regeneration was significantly faster in animals treated with the prepared bigels, with noticeable improvement observed as early as day two.

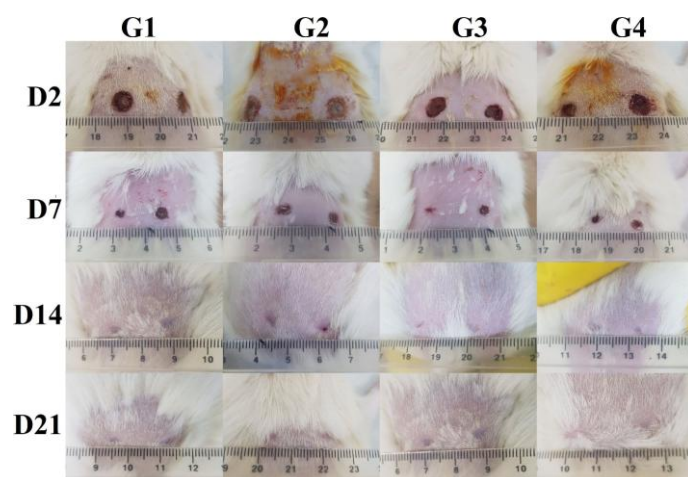


Figure 16. Photographs showing the achieved wound-healing progress. **G1** is the negative control group (untreated animals), and **G2** is the positive control group. The group of animals treated with a gel containing HP-rich *St. John's wort* extract (HP-BG2) is marked with **G3** and that of animals to which HP-NLC-BG2 was applied—with **G4**. The photographs were taken at several post-excision time intervals—two (**D2**), seven (**D7**), fourteen (**D14**), and twenty-one (**D21**) days.

The wound diameter in all experimental animals was accurately measured using an electronic caliper, and the results are presented in Table 12. The data confirm the visual observations made during the study. The therapeutic effect established on the second day was most significant in experimental groups 3 and 4. After 14 days of application, the diameter of the wounds in the animals treated with HP-NLC-BG2 was significantly smaller compared to those in the other groups. Although visible regeneration was observed in each experimental group on the twenty-first day, the smallest wound size was recorded in G4 (1.500 ± 0.548 mm).

Table 12. Wound size during the experiment. The table also shows the initial wound size (**D0**). The results are presented as the mean of seven measured diameters \pm SD.

Research period, days	Mean wound diameter, mm			
	G1	G2	G3	G4
D0	6.000 ± 0.000^a	6.000 ± 0.000^a	6.000 ± 0.000^a	6.000 ± 0.000^a
D2	5.250 ± 0.274^b	4.667 ± 0.517^c	3.917 ± 0.585^d	$3.750 \pm 0.524^{d,e}$
D7	$4.750 \pm 0.274^{b,c}$	$3.583 \pm 0.801^{d,e,f}$	$3.333 \pm 0.258^{d,e,f,g}$	$3.000 \pm 0.447^{f,g,h}$
D14	4.683 ± 0.419^c	$3.568 \pm 0.485^{d,e,f}$	$3.287 \pm 0.181^{e,f,g}$	2.435 ± 0.176^h
D21	$2.833 \pm 0.517^{g,h}$	$3.167 \pm 0.983^{e,f,g}$	2.583 ± 0.585^h	1.500 ± 0.548^i

Mean values marked with different letter indices are statistically distinguishable ($p < 0.05$).

4.2. Plasma antioxidant status

The antioxidant activity of HP-NLC-BG2 was assessed using ABTS and MDA methods. In addition to the already described experimental groups (G1-G4), an additional one was included in the assessment of antioxidant status, designated as a healthy control (G0) and consisting of seven experimental animals with no wounds formed.

Antioxidant capacity

ABTS analysis showed that untreated animals had lower plasma antioxidant capacity than healthy animals, indicating skin wounds act as a source of free radicals (Figure 17). HP-rich *St. John's wort* extract-containing bigels improved antioxidant status compared to untreated animals on the seventh, fourteenth, and twenty-first days, with HP-BG2 and HP-NLC-BG2 also showing more pronounced effects than the reference product. On day 21, antioxidant capacity in G3 and G4 was

lower than G0 but higher than G1, likely due to the concentration-dependent pro-oxidant activity of antioxidants, as seen in previous studies with St. John's wort extracts.

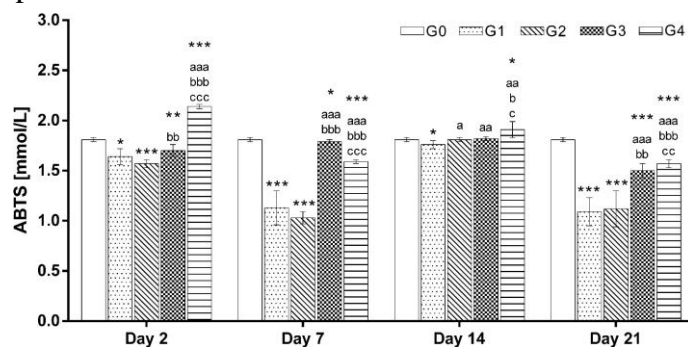


Figure 17. Plasma antioxidant capacity of healthy experimental animals (G0) and the assigned experimental groups (G1–G4). The averaged values obtained from triplicate measurements in the four post-excision intervals—D2, D7, D14, and D21, are presented. Indices represent statistically significant differences: *—compared to G0; a—compared to G1, b—compared to G2; c—compared to G3. The level of statistical significance is reflected by the number of signs—one ($p < 0.05$), two ($p < 0.01$), or three ($p < 0.001$).

Degree of oxidative stress

MDA levels were elevated in untreated animals on days 2 and 7 post-excision but decreased by day 14 to below healthy animal levels (0.34 versus 0.61 nmol/L) (Figure 18). The prepared bigels did not improve MDA levels, which remained higher than in the negative control throughout the study. On days 2 and 7, MDA levels in G3 and G4 were higher than in G2, and after 21 days, the commercial product significantly lowered MDA levels compared to all other groups.

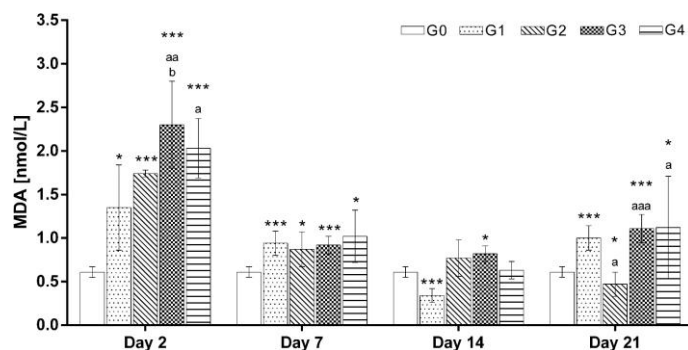


Figure 18. Degree of oxidative stress in the studied groups of experimental animals (G0–G4). The averaged values obtained from triplicate measurements in the four post-excision intervals (D2, D7, D14, D21) are presented. Indices represent statistically significant differences: *—compared to G0; a—compared to G1, b—compared to G2; c—compared to G3. The level of statistical significance is reflected by the number of signs—one ($p < 0.05$), two ($p < 0.01$), or three ($p < 0.001$).

V. Conclusions

1. The influence of the used plant substance and extractant (anhydrous dichloromethane) quantities on the HP concentration in St. John's wort extracts obtained by 48-h maceration under argon ambiance in the absence of light, was established. As the solid-to-solvent ratio increased (from 1:2.5 to 1:3.33), the extraction yield of the desired phloroglucinol rose (from approximately 25% to over 40%).
2. The effect of the experimental conditions (homogenization speed, ultrasonication duration and temperature) on the average particle size, particle size distribution, zeta potential, and stability of NLC carriers (composed of glyceryl behenate/beeswax and almond oil/borage oil) developed by high-shear homogenization/ultrasonication, was reported. The higher homogenization speed (15,000 rpm) led to the destabilization of the lipid nanodispersions. The shorter ultrasound application (5 min) determined a lower degree of uniformity and a larger mean particle size. The different ultrasonication temperatures (4 or 25 °C) did not affect the studied physicochemical characteristics.
3. The inclusion of the extract was successful in two selected nanosamples—HP-NLC3 and HP-NLC4 (composed of glyceryl behenate and almond oil or borage oil). They did not show any visible signs of physical instability within one year of storage at 4 °C. Despite the established statistically significant changes in the physicochemical characteristics of the nanocarriers, the borage oil-based sample (HP-NLC4) retained an average particle size below 200 nm, a polydispersity index less than 0.3, and high zeta potential values $|\gt 35 \text{ mV}|$ and entrapment efficiency ($\gt 50\%$).
4. The incorporation of HP-rich St. John's wort extract did not affect the structural integrity and inner morphology of HP-NLC3 and HP-NLC4. The confirmed absence of lipid polymorphic transitions indicated their stability over time.
5. HP-NLC4 nanodispersion, consisting of glyceryl behenate and borage oil, was characterized by a more pronounced microbicidal effect against *K. pneumoniae*, *S. aureus*, *C. albicans*, and HSV-1 compared to HP-NLC3, containing glyceryl behenate and almond oil.
6. The influence of the hydrogel-to-oleogel ratio used for obtaining stable “blank” and HP-NLC4-loaded bigels based on poloxamer 407, borage oil, and sorbitan monostearate was established. With increasing content of the lipophilic phase, the spreadability and hardness of “blank” bigels, along with the cohesiveness and adhesiveness of HP-NLC4-containing biphasic vehicles, also rose. The rheological behavior of all obtained semi-solid forms (“blank” and loaded) was found to be pseudoplastic. The bigel with a hydrogel-to-oleogel ratio of 80:20 (HP-NLC-BG2) was distinguished by optimal consistency and structural uniformity.
7. HP-NLC-BG2 was found to be characterized by a pronounced wound-healing effect, confirmed *in vivo* by an excision wound model applied to experimental animals. According to the results obtained from ABTS and MDA analyses, its antioxidant effect was expressed primarily by scavenging free radicals.

VI. Contributions

Contributions of a scientific and theoretical nature

1. The optimal lipid composition (glyceryl behenate and borage oil or almond oil) and experimental conditions for obtaining stable NLCs were established (homogenization speed of 10,000 rpm and ultrasonication at 25 °C for 15 min).
2. For the first time, NLCs, including those based on glyceryl behenate and almond oil/borage oil, were loaded with HP-rich St. John's wort extract (> 40%).
3. An optimal NLC carrier of HP-rich St. John's wort extract (composed of glyceryl behenate, borage oil, polysorbate 80, and sorbitan monooleate) in terms of average particle size and particle size distribution, zeta potential, degree of crystallinity, entrapment efficiency, physical stability, and *in vitro* antimicrobial efficacy and antiviral activity, was formulated
4. For the first time, bigel was used as a semi-solid carrier for the dermal application of NLCs, including those loaded with HP-rich St. John's wort extract.
5. A bigel containing poloxamer 407-gelled HP-NLC4 nanodispersion, borage oil, and sorbitan monostearate, with optimal mechanical and rheological characteristics for application to the skin, was formulated.

Contributions of a scientific and applied nature

1. An original protocol for obtaining a St. John's wort extract with a high HP content (> 40%), including 48-h maceration in the dark under argon ambiance at a plant material-to-extractant (anhydrous dichloromethane) ratio of 1:3.33, was developed.
2. An innovative semi-solid dosage form was prepared—a combination of biphasic gel and NLCs (gelled with poloxamer 407 lipid nanodispersion and borage oil structured with sorbitan monostearate), which allows the dermal application of HP-rich St. John's wort extract and provides accelerated wound healing compared to a reference herbal product.